JOURNAL OF GEOPHYSICAL RESEARCH, VOL. 114, A07224, doi:10.1029/2009JA014312, 2009

The Io UV footprint: Location, inter-spot distances and tail vertical extent

B. Bonfond,[1] D. Grodent,[1] J.-C. Gérard,[1] A. Radioti,[1] V. Dols,[2] P. A. Delamere,[2] and J. T. Clarke[3]

Received 2 April 2009; revised 18 May 2009; accepted 19 May 2009; published 31 July 2009.

[1] The Io footprint (IFP) consists of one or several spots observed in both jovian hemispheres and is related to the electromagnetic interaction between Io and the magnetosphere. These spots are followed by an auroral curtain, called the tail, extending more than 90° longitude in the direction of planetary rotation. We use recent Hubble Space Telescope images of Jupiter to analyze the location of the footprint spots and tail as a function of Io's location in the jovian magnetic field. We present here a new IFP reference contour—the locus of all possible IFP positions—with an unprecedented accuracy, especially in previously poorly covered sectors. We also demonstrate that the lead angle - the longitudinal shift between Io and the actual IFP position - is not a reliable quantity for validation of the interaction models. Instead, the evolution of the inter-spot distances appears to be a better diagnosis of the Io-Jupiter interaction. Moreover, we present observations of the tail vertical profiles as seen above the limb. The emission peak altitude is ~900 km and remains relatively constant with the distance from the main spot. The altitudinal extent of the vertical emission profiles is not compatible with precipitation of a mono-energetic electron population. The best fit is obtained for a kappa distribution with a characteristic energy of ~70 eV and a spectral index of 2.3. The broadness of the inferred electron energy spectrum gives insight into the physics of the electron acceleration mechanism at play above the IFP tail.

Citation: Bonfond, B., D. Grodent, J.-C. Gérard, A. Radioti, V. Dols, P. A. Delamere, and J. T. Clarke (2009), The Io UV footprint: Location, inter-spot distances and tail vertical extent, *J. Geophys. Res.*, *114*, A07224, doi:10.1029/2009JA014312.

1. Introduction

[2] The Io UV footprint is the auroral signature of the electromagnetic interaction between Io and the jovian magnetosphere. In each hemisphere, it consists of a main spot together with secondary upstream or downstream spots, (i.e. westward or eastward of the main spot, respectively) and a downstream trailing tail [*Clarke et al.*, 1996, 1998, 2002, 2004; *Prangé et al.*, 1996, 1998; *Gérard et al.*, 2006; *Bonfond et al.*, 2007, 2008]. The root cause for the interaction is the motion of Io with respect to the plasma torus, which generates Alfvén waves propagating along the magnetic field lines that connect Io's neighborhood and Jupiter [see review in *Saur et al.*, 2004].

[3] The propagation of these waves has been historically described by two competing models. The first model proposed is called ''the steady state unipolar inductor model'' [*Goldreich and Lynden-Bell*, 1969] at a time where the existence of neither the Io atmosphere nor the plasma torus had been observationally established. The electric current flowing through Io's atmosphere propagates along field lines to the northern and southern ionospheres of Jupiter, where it closes via the locally horizontal Pedersen current, thus forming a current loop connecting the satellite to the planet. The basic assumption of the model is that an Alfvén wave created at Io would be fast enough to reach the ionosphere of Jupiter and bounce back to intercept Io, establishing this steady current loop. The discovery of the dense plasma torus encompassing the orbit of Io challenged the assumptions of the unipolar inductor model. The high plasma density would slow tremendously the propagation velocity of the Alfvén wave originating from Io. If this wave retardation is strong enough, then, by the time the wave is reflected from Jupiter's ionosphere back to the torus, Io would have had time to slip free from the magnetic flux tube which intercepted it at the time the wave was originally launched. Consequently, the interaction in this picture is better described in terms of propagation of MHD Alfvén waves which form ideal Alfvén wings. This type of wave carries a current approximately field-aligned, which does not require a closure in Jupiter's ionosphere [*Neubauer*, 1980]. Detection by the Galileo spacecraft of a quasi-stagnated flow in the wake of Io, within half an Io radius of the surface [*Frank et al.*, 1996], regenerated interest in

[1]Laboratoire de Physique Atmosphérique et Planétaire, Université de Liège, Liege, Belgium.
[2]Laboratory for Atmospheric and Space Physics, University of Colorado, Boulder, Colorado, USA.
[3]Department of Astronomy and Center for Space Physics, Boston University, Boston, Massachusetts, USA.

0148-0227/09/2009JA014312$09.00

the unipolar inductor model in the literature: because of the strongly retarded flow, the Alfvén wave launched at Io could have the time to bounce back from the ionosphere and return to Io, which is the scenario of the unipolar inductor. Several authors recently proposed a formalism where the Alfvén wing model and the unipolar inductor are the two extreme cases of the same interaction [*Crary and Bagenal*, 1997; *Pontius*, 2002; *Saur*, 2004].

[4] In principle, careful observations of the location of the Io spot could determine whether the interaction is better described with either the unipolar or the Alfvén framework, or a potential mix of the two. The distance between the observed IFP auroral emission and the instantaneous projection of Io on the jovian ionosphere along the field lines is called the "lead-angle". The unipolar inductor model predicts a large lead angle $\geq 12°$, depending on the conductivities of Io and Jupiter but not on the location of Io in the torus. The Alfvén wings model predicts a smaller lead angle $\leq 6°$, independent of the jovian conductivity but strongly dependent on the local plasma properties through which the Alfvén wave is traveling. Consequently the Alfvén wing model is strongly dependent on Io's latitudinal location in the torus. In both cases, the IFP is expected to occur downstream (along the direction of planetary rotation) of the position of Io as mapped along undisturbed magnetic field lines.

[5] The first estimates of the lead angle were based on IR images and on the O6 magnetic field model [*Connerney et al.*, 1993]. They suggested that the lead angle was independent of Io's System III (S3) longitude and was as large as $15-20°$. These results were in favor of the unipolar inductor. However, *Clarke et al.* [1996, 1998], *Prangé et al.* [1998] and more recently *Gérard et al.* [2006] showed lead angle measurements based on HST FUV observations and on O6 or on VIP4 magnetic field models [*Connerney et al.*, 1998] indicating that the lead angle could vary with Io's longitude and even attain negative values. This later result is particularly puzzling since no model predicts an upstream bending of field lines or a perturbation which propagates against the rotation of ambient magnetospheric plasma. The occurrence of lag angles was attributed to the lack of accuracy of the magnetic field longitudinal mapping. The VIP4 magnetic field model and its later improvements by *Grodent et al.* [2008] are built in such a way that the mapping of the Io orbit along the field lines is constrained to fall on the locus of the IFP as seen on IR or UV images (the IFP reference contour). This method brings substantial improvements compared to earlier models which relied only on in situ magnetic field measurements in the equatorial plane. However, the longitude along the reference contour is not constrained by the observations. If the magnetic field models were directly linking Io to its northern and southern footprints by construction, then measurements of the lead angle would be meaningless. Nevertheless, it is not clear whether the absence of such a constraint provides more significant information.

[6] Another method to determine the lead angle is based on measurements of the inter-spot distances. If the Alfvénic perturbations remain small compared to the ambient field, then the lead angle is directly linked to these distances. The relationship between secondary spot positions and Io's centrifugal latitude (i.e. latitude with respect to the rotational equator) was first suggested to be caused by reflections of the Alfvén waves on the torus boundaries [*Gérard et al.*, 2006]. In this case, the maximum lead angle is expected to correspond to half of the maximum inter-spot distance. However the recent finding of a faint spot appearing upstream of the main emissions puts this interpretation into question. An alternative explanation assumes that the upstream or downstream secondary spots are caused by electron beams originating from the opposite hemisphere [*Bonfond et al.*, 2008]. According to this trans-hemispheric electron beams model, when Alfvén waves dissipate their energy in the form of electron parallel acceleration, most electrons are accelerated towards the planet, creating the main Io spot. Part of the electron population, however, is accelerated towards the opposite hemisphere in the form of electron beams. Since these electrons are essentially undisturbed by the torus plasma (unlike the Alfvén waves), they may precipitate upstream or downstream of the other hemisphere's main spot depending on the Io centrifugal latitude. Three spots are defined in this framework: the Main Alfvén Wing spot (MAW spot), the Trans-hemispheric Electron Beam spot (TEB spot) and the Reflected Alfvén Wing spot (RAW spot). Accordingly, the maximum inter-spot distance between the MAW spot and the TEB spot would provide a good estimate of the maximum lead angle. Nevertheless, other models considering a stronger interaction do not predict such obvious relationships between the inter-spot distance and the lead angle. It is not clear how a pure unipolar model could explain the multi-spot structure and the systematic variation of the inter-spot distances. However, *Jacobsen et al.* [2007] suggested that strong non-linearities could trigger wave interference patterns leading to the occurrence of multiple spots and depending on Io's location in the torus.

[7] The large Hubble Space Telescope (HST) campaign dedicated to Jupiter's aurora in Spring 2007 brought a wealth of new data concerning the IFP. In the first part of this article (section 3), we describe the careful determination of the footprint location. We define a new IFP reference contour, and careful measurements of the lead angles as well as of the inter-spot distances on an unprecedented longitude coverage.

[8] In the second part (section 4), we address another structure of the Io footprint: the long auroral tail downstream of the spots. This tail extends over more than 90° of longitude. Based on UV spectroscopy and a model of electron transport in the atmosphere of Jupiter, *Gérard et al.* [2002] determined that the impinging electrons that excite the tail emissions have a mean energy $\sim$55 keV when the electron distribution function is assumed to be Maxwellian. They also determined that although the brightness of the tail decreases slowly as the distance from the main spot increases, the electron energy deduced from spectroscopy was roughly constant along the tail and the brightness decrease was thus mainly caused by a decreasing particle flux. There are currently few models addressing the tail electrodynamics and all of them assume a steady state. They assume that the tail is the auroral signature of the horizontal divergence of the current crossing the Io plasma wake. This current is needed to reaccelerate the flux tubes, slowed through mass loading by Iogenic plasma, to almost full corotation. *Hill and Vasyliūnas* [2002] apply the same

approach as the one proposed for the unipolar inductor model. The jovian Pedersen conductivity limits the current in the loop connecting the plasma wake of Io and the jovian ionosphere. Finite ionospheric conductivity thus impedes the return to corotation of the plasma behind Io. *Delamere et al.* [2003] compute the momentum transfer between the plasma in the torus and the plasma slowed by its interaction with Io's atmosphere. After this momentum transfer, they compute a residual potential drop across the Io flux tube $\sim$70 kV. They note that if the auroral electron had to be accelerated by a static potential structure parallel to the field line to the $\sim$55 keV proposed by *Gérard et al.* [2002], then most of the $\sim$70 kV cross-flux tube potential drop available has to be used for this acceleration. They conclude that the corresponding horizontal electric field in Jupiter's ionosphere is thus small and that the Pedersen conductivity is not relevant. Contrary to Hill and Vasyliunas, they conclude that the plasma in the wake of Io is highly decoupled from the jovian ionosphere. *Ergun et al.* [2009] used the Hill and Vasyliunas approach but added an equation describing the quasi-static potential drop along the magnetic field lines, using a current-voltage relation derived by *Knight* [1973]. The Knight current-voltage relation is modified in the model of *Ergun et al.* [2009] to take into account the low plasma density at the foot of the flux tube that limits the parallel (field aligned) current. *Ergun et al.* [2009] compute self-consistently a precipitated electron energy flux $\sim$1 mW/m^2 compatible with the UV observations, a tail extension comparable to the one deduced by Hill and Vasyliunas (see section 4.3), and a precipitated electron energy $\sim$1 keV, much lower that the $\sim$55 keV estimation of *Gérard et al.* [2002].

[9] Some images from the large database used for this work show the Io tail emission in such a configuration that its vertical profile can be directly measured. The position of the extracted profiles relative to the main spot was deduced using our new IFP reference contour. We present new measurements describing how the brightness, the peak altitude and the vertical distribution of the tail emissions evolve with the distance from the main spot. We also use a Monte Carlo model of the energy degradation of the auroral electrons precipitating into a theoretical jovian atmosphere in order to compute the UV emission rates from excited H_2 and H. By comparing the simulated emission rates and profiles with the observed ones we deduce the energy distribution of the precipitated electron flux. Consequently, the brightness profiles provide information on the precipitated electrons energies. This technique is therefore independent of the spectral color ratio method [*Gérard et al.*, 2002]. Additionally, this deduced energy distribution gives insight into the physical process accelerating the electrons that we compare with the processes proposed in the models explaining the IFP tail described earlier in this introduction.

2. Data Processing

2.1. Data Sets and Reduction

[10] This work is based on the HST images gathered during the HST/New Horizons campaign (GO 10862) which took place from 20 February to 11 June 2007. We used the Multi-Anode Microchannel Array (MAMA) detector of the Advanced Camera for Surveys (ACS) Solar Blind Channel (SBC) in order to image the far ultraviolet (FUV) auroral emissions of Jupiter. 517 images have been acquired with the F115LP filter which includes H_2 Lyman and Werner bands as well as the 121.6 nm H Lyman-α line. Similarly, 1001 images have been acquired with the F125LP filter which includes the same H_2 bands as the previous filter, but excludes the Ly-α line. This filter provides a better signal-to-noise ratio since it rejects most of the geocoronal emissions. A typical observation orbit consists of 19 images with 100-second exposure times. The first 5 use the F125LP filter, the next 9 use the F115LP filter and the last 5 use the F125LP filter again. In addition, 11 orbits were specifically dedicated to the Io footprint and consisted of sets of 30-second exposures acquired with the F125LP filter alone. We performed dark current, flat field and geometric corrections so that each pixel edge subtends an angle of 0.0301 arcsec once the data have been treated by the image processing pipeline. Since the Earth-Jupiter distance ranged from 8×10^8 to 6.5×10^8 kilometers (i.e. from $\sim$5.3 to $\sim$4.3 AU) during the observation campaign, the pixel size corresponded to 120 km at the beginning of the campaign and to 94 km at the end.

[11] Our limb fitting method (see next section) was tested on images of Saturn acquired during the same observation campaign with the same instrument and the same set of filters. We processed these images in an identical way as for Jupiter and the usual pixel size corresponds to 180 km at Saturn during this campaign.

2.2. Planetary Center Localization

[12] The limited accuracy of the HST guide star catalogue and the uncertainty in the start time of the tracking motion prevent us from precisely locating the center of Jupiter on the images just from pointing information. However, the determination of the planetary center is a mandatory step before locating any structure in the images. Therefore, we developed an automatic procedure based on the detection of the planetary limb to compute the planetary center. Should the filter perfectly isolate the H_2 and H UV emissions below 1650 Å, the limb altitude would be related to the UV dayglow emission. However, the planetary disk seen on ACS FUV images mainly results from the reflected solar continuum in longer wavelengths that is leaking into the detector [*Boffi et al.*, 2008]. Consequently, a reasonable assumption is that the limb altitude as detected on the images indeed corresponds to the solar reflection limb with an inflection point located at the 1 bar level, where the 0 km altitude is set and which corresponds to an ellipsoid with an equatorial radius of 71,492 km and a polar radius of 66,854 km. In order to test this hypothesis, we used ACS images of Saturn acquired with the same filters. On these images, the planetary center can be computed with an independent method, i.e. by fitting the A, B and C rings in lieu of relying on the planetary limb [*Gérard et al.*, 2009]. Elliptic bands, whose dimensions are deduced from ephemerides and from the detector plate scale, are adjusted to the observed rings. The center of these ellipses provides an excellent estimate of the planetary center, with an accuracy of $\sim$1 pixel. We then perform radial scans of the day-side limb and compute the altitude of the inflection point given the center location from the ring fitting (Figure 1). The mean altitude of the inflection point is measured at 0°, 45°S

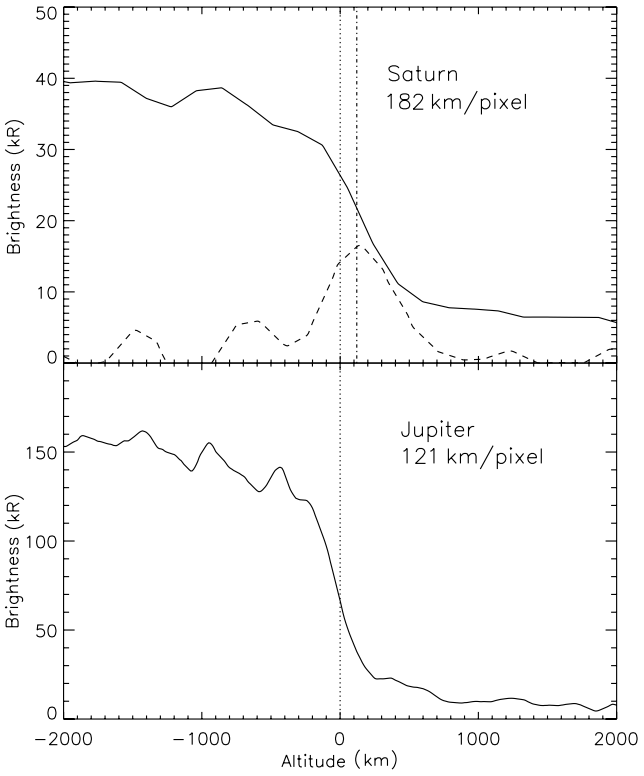

Figure 1. Example of an equatorial limb profile at (top) Saturn and at (bottom) Jupiter. The dashed line represents the altitude derivative of the brightness profile. The dotted line represents the 1 bar level, corresponding to 0 km. On Saturn, the altitude of the inflection point (highlighted by the dash-dotted line) is smaller than the pixel size.

and 65°N latitudes on the sunlit side of the planet. In the three cases, the mean altitude is almost within a pixel from the 1 bar level (see Table 1).

[13] Since the atmospheric composition of both giant planets is similar, we expect that the conclusions drawn about the altitude of the inflection point at Saturn are applicable to Jupiter as well. Consequently, our limb-fitting method at Jupiter consists of scanning the imaged jovian limb while rotating the image following one degree steps around the planetary center, looking for the inflection point in the altitudinal intensity profile. In order to perform these scans, we first need to perform an initial guess of the center location based on a rough estimate of the position of the planetary disk on the image. We then build a mask to exclude the points poleward of the Io footprint contour, so that auroral emission does not contaminate the brightness profiles. Points on the terminator side are shifted in order to take the angle between the Sun and the Earth directions into account. The last step consists of fitting the computed points with the theoretical elliptical projection of the limb deduced from the ephemerides and the known pixel size. The fitted center of this ellipse thus corresponds to the planetary center on the image.

3. Location of the Io Footprint

3.1. New Io Reference Contours

[14] IR and UV observations have shown that the IFP follows a fixed path in S3, called the IFP reference contour. In order to fully determine this contour in each hemisphere, we need images of the IFP spanning all Io S3 longitudes. In previous HST campaigns, the observing geometry was mainly constrained by the visibility of the main auroral emission, systematically leaving some configurations unexplored. The latest ACS observations now fill most of these gaps and provide the missing data points. *Grodent et al.* [2008] used this more complete ACS dataset to build reference contours for Io, Europa and Ganymede in the northern hemisphere by selecting manually the location of the footprint spots and Io's tail on the images. Following *Grodent et al.* [2008], we assume the manually selected spots to be located 700 km above the 1 bar level. These observations include configurations where the IFP lies very close to the planetary limb, leading to large inaccuracies. The problem is particularly pronounced in the 350–100° Io S3 sector, where the reference contour does not seem to form a closed curve according to the simple polar projection of the observed footprint location (see Figure 1 in *Grodent et al.* [2008]). In order to increase the accuracy of the IFP localization in this critical sector, we take advantage of the fact that our observations were designed to acquire images in the same Io S3 longitude but for different local time configurations. The Io S3 longitude difference tolerance between the two observations is as low as 0.25°, which is less than one third of the S3 longitude range covered by Io in 100 s. This means that, for each pair of images, Io is almost in the same position with respect to the jovian magnetic field, but the footprint is seen from different points of view (with respect to the Jupiter-Earth line of sight). Assuming that the IFP is located exactly at the same place on both images, we determine the longitude/latitude couple that minimizes the distances in pixels between the computed point and the manually selected pixel on both images. The new IFP location typically lies within 2–3 pixels of the originally selected position. For example, the uncertainty on the IFP location around 0° Io S3 longitude, which was as large as 5° based on single images, is now reduced down to ~2° in longitude and ~1° in latitude. In the sectors where such image pairs exist, we only take these new points into account (pale grey triangles in Figure 2). In sectors where images pairs are missing, we consider spot locations (dark grey diamonds) or tail locations (black crosses) derived from unique images. We are now in position to construct a new reference contour with a more realistic closure in the northern 30–60° Io S3 longitude range (Figure 2a and Table 2). The agreement between our reference oval and the footprint positions measured on high resolution images (from 25.7 km/pixel to 133.7 km/pixel) in the visible wavelength by Galileo [*Vasavada et al.*, 1999] is convincing. We note that, in the North, our reference

Table 1. Mean Altitude of the Radial Light Curve Inflection Points on Saturn Measured From the 1-bar Level[a]

	Mean (km)	Std. dev. (km)
Equator	157	215
45°S	11	169
65°N	−74	101

[a]Since one pixel subtends 180 km, we note that the mean altitude as well as the standard deviation of this altitude are on the same order or lower than the pixel size.

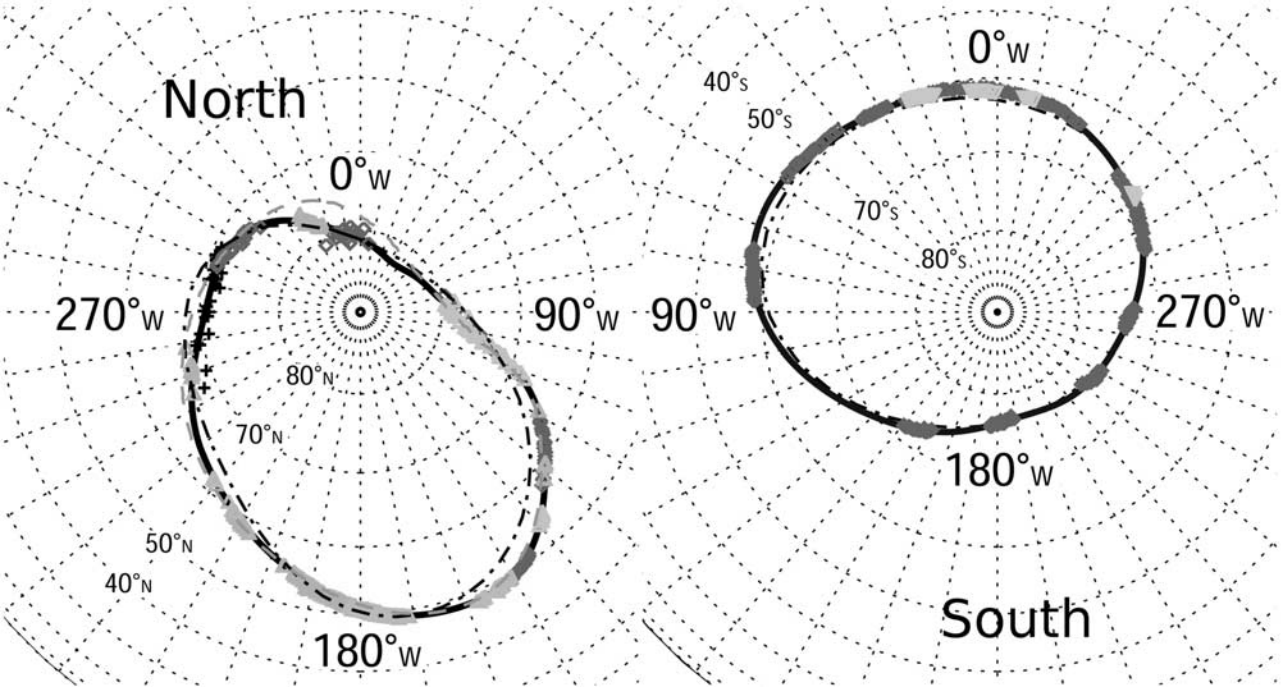

Figure 2. Planeto-centric polar projection of the Io reference contours for the northern and the southern hemispheres. The triangles represent IFP locations computed from coupling two images. The rhomboids represent IFP locations deduced from a unique image. The black crosses represent points selected in the IFP tail. The black dash-dotted line is the IFP contour from the VIP4 model, the dashed grey line is the IFP contour from the second model described in *Grodent et al.* [2008] and the thick plain black line is the best fit to the points described above.

contour mainly differs from the VIP4 Io contour in the region influenced by the magnetic anomaly between 100 and 180° longitude. Some significant differences also arise between 210° and 290°.

[15] As far as the southern hemisphere is concerned, the Io S3 coverage gaps were even wider than in the North. Most of them are now filled, making it possible to draw an updated southern Io footpath reference (Figure 2b and Table 2). The agreement between the VIP4 Io contour and our reference contour is better in the South. Our footpath only lies a few degrees equatorward from the VIP4 contour near 0° and near 90°. Finally, we note that the two contours have very similar lengths: ~173,000 km for the North and ~167,000 km for the South.

3.2. Lead Angle and Inter-Spot Distances

[16] Now that we have an accurate relationship between the orbital longitude of Io and the corresponding position of the main IFP spots, computing the lead angles is relatively straightforward provided we have an accurate magnetic field model. In addition to the VIP4 model, we also used the second octupole + dipole model from *Grodent et al.* [2008] in the North for comparison. It should be noticed that, where the northern contour is very close to the pole, a small distance on the planet corresponds to a huge interval when expressed in terms of longitude. Moreover, measuring the longitudinal shift directly on the planet does not enable us to meaningfully compare values from opposite hemispheres nor to verify theoretical predictions since these usually implicitly assume an axisymmetric magnetic field. Consequently, in order to avoid these geometrical effects due to the shape of the contours, we provide measurements of the equatorial lead angles. Thus, contrary to *Clarke et al.* [1998] and *Gérard et al.* [2006], we do not magnetically map the location of Io to the ionosphere and then measure the longitudinal distance to the actual IFP. Instead, we link the IFP location to the nearest point on the model reference contour and we map this point back to the equatorial plane in order to measure the actual longitudinal shift with respect to Io. Figure 3a shows that the equatorial lead angle in the North is strongly model dependent. For example, the inexplicable negative lead angles in the 100° sector disappear when the magnetic mapping is done by the *Grodent et al.* [2008] model. Figure 3b shows that the equatorial lead angle in the South has a more structured behavior, showing a smooth evolution as a function of Io's longitude. Nevertheless, the maximum and the minimum lead angles both appear when Io is in the center of the torus, i.e. close to 110° and 290° S3.

[17] In Figure 4, we show the variations of the inter-spot distances for both hemispheres according to the trans-hemispheric electron beam model [*Bonfond et al.*, 2008]. In this plot, points are marked only when the TEB (and the RAW) spots are clearly observed on the image. The distances are shown in kilometers in order to avoid problems with the contour geometry and the use of magnetic field models. However, in order to provide a rough idea of the distances in terms of longitudinal shift, we can consider that 1° corresponds to ~470 km (~480 km in the North and ~465 km in the South). In the North, the secondary spots

Table 2. Planeto-Centric Coordinates of the Io Northern and Southern Reference Ovals[a]

Io S3 Longitude (°)	North IFP Longitude (°)	North IFP Latitude (°)	South IFP Longitude (°)	South IFP Latitude (°)
0	−32.0 ± 2	76.9 ± 1	5.1 ± 1	−61.4 ± 1
10	−22.6 ± 5	78.5 ± 1.5	14.1 ± 1	−61.0 ± 1
20	−2.1 ± 7.5	81.0 ± 2	23.2 ± 1	−60.6 ± 1
30	32.7	82.7	32.2 ± 1.5	−60.1 ± 1
40	70.7 ± 3	81.4 ± 2	40.9 ± 1	−59.3 ± 1
50	96.9 ± 2	77.0 ± 1.5	49.2 ± 1	−58.5 ± 1
60	110.1 ± 1	69.3 ± 1.5	56.9 ± 1	−57.7 ± 1
70	118.6 ± 1.5	64.3 ± 1	64.1	−57.3
80	126.3 ± 1.5	60.9 ± 1	71.0	−57.3
90	132.6 ± 1	57.9 ± 1	77.8 ± 1	−57.7 ± 1
100	137.7 ± 1	55.0 ± 1	84.5 ± 1	−58.6 ± 1
110	142.1	52.6	91.3	−60.0
120	145.8 ± 0.5	50.8 ± 1	98.3	−61.8
130	150.0 ± 0.5	49.5 ± 1	105.5	−63.8
140	154.5 ± 0.5	48.8 ± 1	113.2	−66.0
150	158.4 ± 0.5	48.6 ± 1	121.8	−68.1
160	162.7	48.7	131.6	−70.2
170	168.1 ± 0.5	48.9 ± 0.5	143.3 ± 1.5	−72.1 ± 1
180	173.5 ± 0.5	49.5 ± 0.5	156.8 ± 1.5	−73.9 ± 1
190	178.4 ± 0.5	50.4 ± 0.5	172.1 ± 2.5	−75.6 ± 1.5
200	183.2 ± 1	51.7 ± 0.5	188.6 ± 2.5	−76.8 ± 1.5
210	188.5 ± 1	53.3 ± 1	205.4	−76.8
220	194.3 ± 1	55.0 ± 1	221.7	−76.2
230	200.5 ± 1	56.6 ± 1	236.6 ± 1.5	−75.6 ± 1
240	207.5 ± 1	58.5 ± 1	250.1	−75.0
250	214.6 ± 1	60.4 ± 1	262.0 ± 2	−74.2 ± 1
260	220.8 ± 2	61.6 ± 1	272.8 ± 2	−73.0 ± 1
270	228.0 ± 3	63.0 ± 1	282.9	−71.7
280	238.8 ± 1.5	65.1 ± 0.5	292.6 ± 2.5	−70.4 ± 1
290	252.1 ± 1.5	67.7 ± 0.5	302.2 ± 2	−69.0 ± 1
300	265.4	69.8	311.7 ± 1.5	−67.8 ± 1
310	278.4	70.9	321.0 ± 1.5	−66.5 ± 1
320	290.6 ± 5	71.6 ± 1.5	330.0	−65.2
330	301.5 ± 5	72.5 ± 1.5	338.8 ± 1.5	−64.0 ± 1
340	311.6 ± 5.5	73.9 ± 1.5	347.5 ± 1	−62.9 ± 1
350	320.7	75.5	356.3 ± 1	−62.0 ± 1

[a]Assuming a selection uncertainty of 3 pixels, the mean geometric uncertainty is provided only when it is constrained by data points.

are usually fainter than in the South. Thus these spots can only be distinguished from the main one when the inter-spot distance is large enough. However, between 0° and 100° in the southern hemisphere, the TEB spot becomes as bright as the main one and we can follow their merging on the images. The variations of the southern inter-spot distances look regular and correlated with the position of Io in the torus. Additionally, the inter-spot distances in the North and in the South appear to follow a symmetric behavior (see also Figure 3 in *Bonfond et al.* [2008]).

4. IFP Tail

4.1. Peak Altitude and Vertical Profiles

[18] On several ACS images, we can clearly see the Io footprint, or at least its trailing tail, lying right above the limb (Figure 5). Consequently, we consider here a selection of images where the tail appears crossing the limb plane. These images originate from 10 different HST orbits. For each orbit, the 19 original images are assembled into 7 sets of 3 images (2 images are thus used twice) to increase the signal to noise ratio. The following data reduction steps are performed on the summed images (7 per orbit). We developed a semi-automatic method to perform radial scans of the planetary limb in a manually selected sector and measure the altitude of the emission peak as a function of the rotation angle. If the precipitating particle characteristic energy is constant along the tail, then the emission peak appearing the furthest from the planetary edge lies in the limb plane. Additionally, the radial profile extracted at this location should reflect the actual vertical extent of the emission.

[19] Non-auroral planetary disk emissions also contribute to the low altitude part of the observed profiles. Consequently, we built an empirical disk vertical profile extrapolated from profiles extracted at lower latitudes for each image. We remove this disk emission profile from the total profile in order to keep the auroral emission only. Then we fit the extracted vertical profiles with a Chapman profile of the form:

$$f(Z) = C\exp\left(1 - \left(\frac{Z - Z_0}{H}\right) - \exp\left(-\frac{Z - Z_0}{H}\right)\right) \quad (1)$$

where C is a constant, Z is the altitude in km, Z_0 is the altitude of the peak in km and H is the scale height in km. The scale height of these emissions lies around 430 km ± 70 km and does not depend either on the filter nor on the distance from the main spot.

[20] The mean altitude of the emission peak we derive from the profiles is 900 km ±125 km. Note that the standard deviation is fairly close to 120 km, which is the typical distance subtended by one pixel on Jupiter. This indicates that the variability due to measurement uncertainty provides an upper limit to the real, intrinsic fluctuations. Figure 6

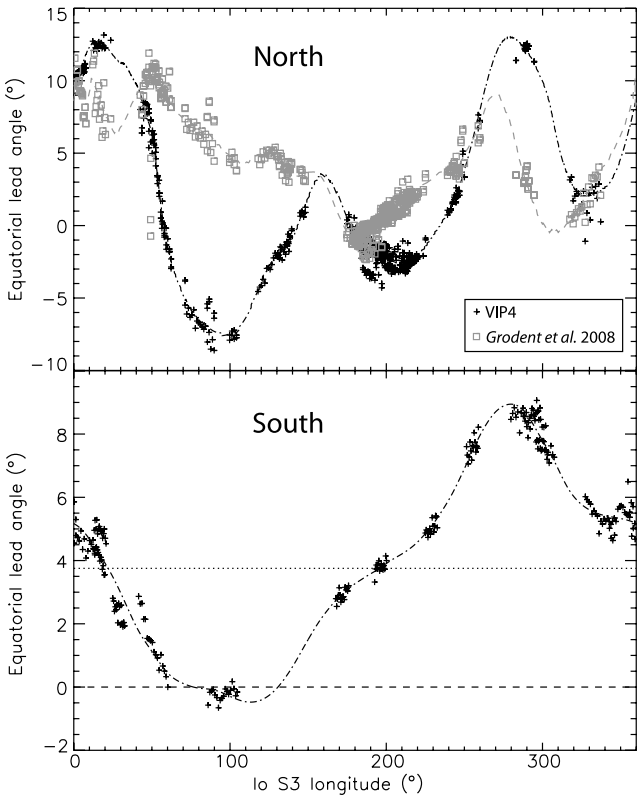

Figure 3. Equatorial lead angles for the northern and the southern footprints. The black crosses represent the data points as computed with the VIP4 model while the grey squares represent the equatorial lead angle using mapping from the second octupole + dipole model from *Grodent et al.* [2008]. The black dash-dotted and grey dashed curves are fifth order Fourier series fitting of the data points for the VIP4 and *Grodent et al.* [2008] models respectively.

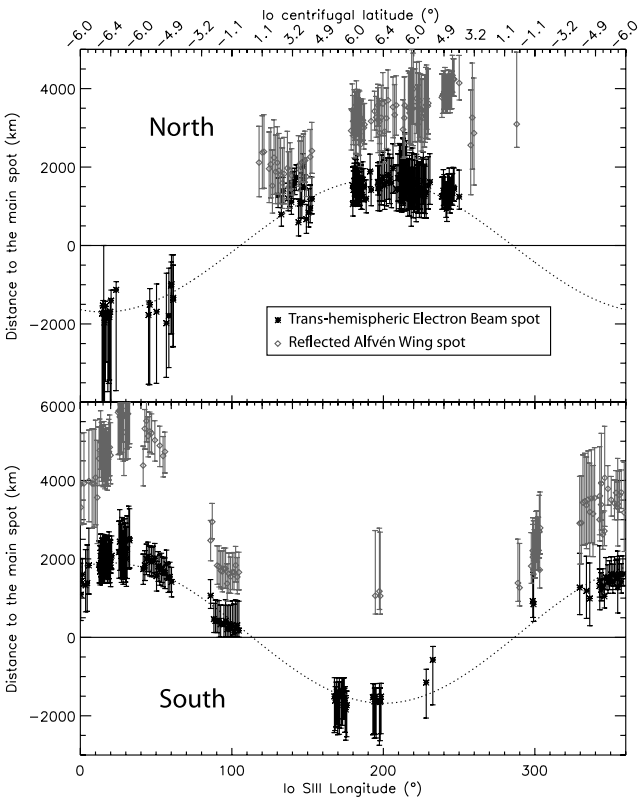

Figure 4. Inter-spot distances as a function of the Io S3 longitude of the (top) northern and the (bottom) southern hemispheres. The error bars are built assuming a selection uncertainty of 1 pixel for the main spot and 2 pixels for the usually fainter secondary spots. The adopted theoretical framework to decide which is the main spot is the same as in *Bonfond et al.* [2008]. The two curves correspond to the best fit of the points with a sinusoid function. The maxima lie around 1500–2000 km which roughly corresponds to 3–4° into the equatorial plane.

shows the variation of the peak altitude as a function of the longitudinal distance from the Io footprint main spot according to the reference contour described above. The distances are expressed in kilometers along the reference contour to avoid complications owing to the contour geometry. From the length of the reference contours, 2000 km roughly corresponds to ∼4° in the equatorial plane. Consequently, the furthest points on this plot are approximately 60° away from the main spot. The further the profile stands from the main spot, the higher is the altitude of the brightness peak. However, the correlation coefficient is only 0.09 and is not significantly different from 0 for a confidence interval of 99%. This result justifies a posteriori our initial assumption of the constant altitude of the auroral curtain.

4.2. Estimate of the Energy Distribution

[21] The emission peak altitude provides an estimate of the precipitating particle energy and it puts a strong constraint on the electron acceleration mechanism. Additionally, the emission profile reflects the shape of the energy spectrum. We selected a sub-set of images coming from two consecutive HST orbits acquired on 24 February 2007 in the southern hemisphere to build a typical vertical profile of the tail. This set of 38 images has been chosen because the

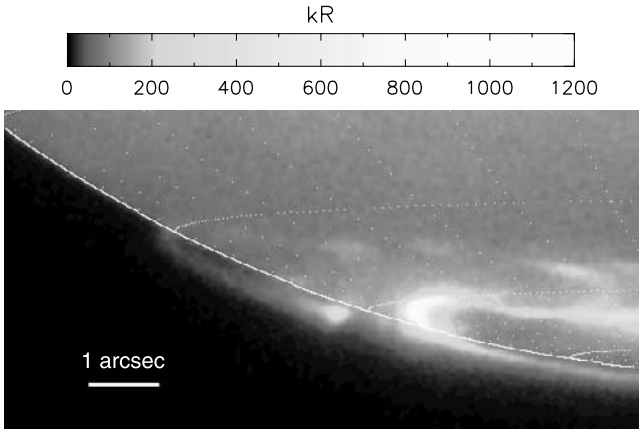

Figure 5. Example of Io footprint tail seen right above the limb plane in the southern hemisphere. The reference ellipsoid, where the 0 km altitude is set, has an equatorial radius of 71,492 km and a polar radius of 66,854 km. Parallel and meridian lines are drawn every 10°.

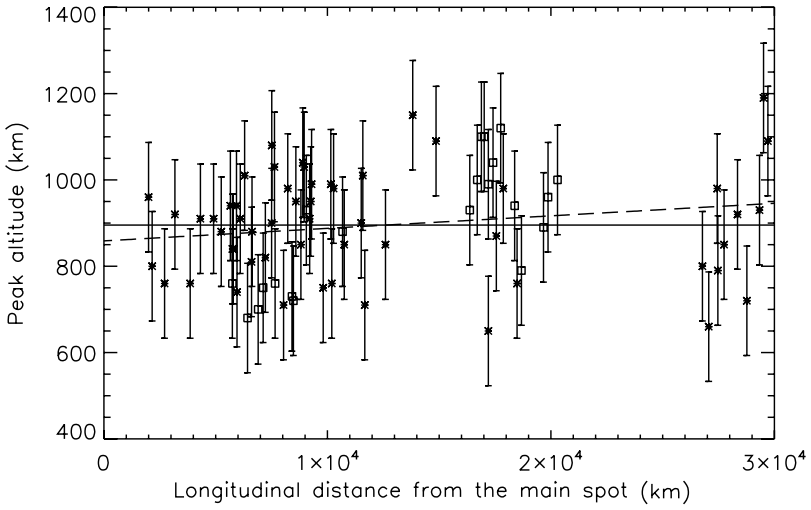

Figure 6. Altitude of the peak of the brightness profiles as a function of the distance of this profile from the IFP main spot location as described by our new reference contours. The stars and squares are for points in the northern or the southern hemisphere respectively. The mean altitude is 900 km and the increase of the peak altitude is not statistically significant. This indicates that the precipitating electron energy is relatively constant with the distance to the main spot.

curtain is quasi-perpendicular to the observer and because auroral diffuse emissions do not contaminate the lower altitude part of the profile. We sum these 38 profiles to generate a typical observed profile with a signal to noise ratio as large as possible ($\frac{S}{N} \simeq 12$ in lieu of $\sim$2 for single images) and we compare it to different theoretical emission profiles. Spectral measurements showed that hydrocarbon absorption of the IFP FUV emissions was measurable but relatively weak [*Gérard et al.*, 2002]. However, we have very little observational information on the methane vertical distribution in the polar regions. Consequently, we consider that hydrocarbon absorption does not significantly affect the shape of the emission vertical profile.

[22] The numerical model used to calculate electron transport in planetary atmospheres has been described in detail by *Shematovich et al.* [2008]. The incident electrons lose their excess kinetic energy in elastic, inelastic and ionization collisions with the ambient atmospheric gas consisting of H_2, He, and H. If the collision produces ionization, a secondary electron is created and is randomly assigned an isotropically distributed pitch angle and an energy in accordance with the procedure given by *Garvey and Green* [1976], *Jackman et al.* [1977] and *Garvey et al.* [1977]. The cross sections and scattering angles used to calculate the energy loss associated with elastic and inelastic collisions of electrons with H_2, He, and H were taken for H_2 from the AMDIS database (https://dbshino.nfs.ac.jp) and *Shyn and Sharp* [1981]; for He and H from the NIST database (http://physics.nist.gov/PhysRefData/Ionization/) and *Jackman et al.* [1977], *Dalgarno et al.* [1999]. Their transport is described by the kinetic Boltzmann equation. The Direct Simulation Monte Carlo (DSMC) method is used to solve atmospheric kinetic systems in the stochastic approximation [see *Shematovich et al.*, 2008 and references therein]. The lower boundary is set at an altitude 0.25 μbar and the upper boundary is fixed at 6.5×10^{-11} μbar where the atmospheric gas flow is practically collisionless. The region of the atmosphere under study is divided into 49 vertical cells uniformly distributed on a logarithmic pressure scale. The evolution of the system of modeled particles due to collisional processes and particle transport is calculated from the initial to the steady state. The pressure-altitude relationship from *Grodent et al.* [2001] is adopted because it is the most realistic auroral atmosphere available. For a given initial mono-energetic beam, the model provides a vertical emission profile assuming an isotropic pitch angle distribution at the top of the atmosphere.

[23] If we consider a mono-energetic distribution, the curve that best fits the observations has a typical energy of 2 keV (Table 3). However, even after taking the point spread function (PSF) of the ACS camera into account, its vertical width is too small to reasonably reproduce the observations. Because of the curvature of the planet, an extended emission region leads to an apparent broadening of the emission profile. A simulation of the emission integration along the line of sight shows that the size of the emission region should be 20 times larger than the vertical scale height to generate significant effects. In our case, we determine that the curtain latitudinal width corresponds to the projected diameter of Io and lies between 100 and 200 km, i.e. only 0.25 to 0.5 times the observed scale height ($\sim$400 km). Consequently, we may conclude that the width of the vertical emission profiles is due to a broad distribution in the energy of the precipitating electrons. We tested three different energy distributions in order to obtain information on the shape of the particle energy spectrum: a Maxwellian distribution

$$I = CE \exp\left(\frac{-E}{E_0}\right), \tag{2}$$

a power law distribution

$$I = CE^{-\gamma} \tag{3}$$

Table 3. Parameters of the Best Fit Curves Compared to the Summed Profile Aquired ~20° Away From the Main Spot[a]

Distribution	Characteristic energy (E_0)	Spectral index (γ or κ)	Mean energy
Mono-energetic	2 keV (1.3 keV)	-	2 keV (1.3 keV)
Maxwellian	960 eV (540 eV)	-	1.9 keV (1.1 keV)
Kappa	70 eV (75 eV)	2.3 (2.4)	1.1 keV (0.8 keV)
Power-law	-	1.9 (1.8)	-

[a]The numbers between brackets are computed for a point located approximately 40° away from the spot. The mean energy is computed as the ratio of the energy flux $\int_0^\infty EI\,dE$ over the particle flux $\int_0^\infty I\,dE$.

and a kappa distribution

$$I = CE(E + E_0\kappa)^{-1-\kappa} \tag{4}$$

where I is the differential intensity in $cm^{-2}\ s^{-1}\ sr^{-1}\ keV^{-1}$, E is the electron energy in *keV*, C is a constant, E_0 is the characteristic energy in *keV*, and γ and κ are the spectral indices of the power-law and the kappa distributions, respectively. For each distribution, we divide the energy range between 30 eV and 30 keV into 30 energy bins (uniformly distributed on a logarithmic energy scale) in which we compute the mean and total energies. We simulate an emission profile for each energy bin with the Monte Carlo model. Finally we weight the emission profiles with the channel total energy and we sum them to generate the emission profile corresponding to the adopted distribution and set of parameters. After smoothing the profile with a boxcar function of the size of the PSF, we perform a least squares fit to compute the best parameter set for each energy distribution. The results are given in Table 3. Figure 7 shows the best simulated vertical profiles and compares

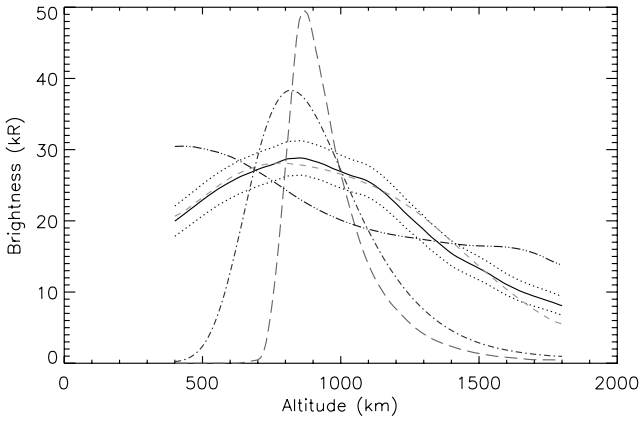

Figure 7. Observed and simulated vertical emission profiles. The observations and the estimated uncertainties are represented by the solid line surrounded by the dotted lines. The four other lines are the best fit vertical profiles based on the theoretical distributions described in the text. The long dashed line corresponds to the mono-energetic distribution, the small dashed line corresponds to the kappa distribution, the dash-dotted line corresponds to the Maxwellian distribution and the dash-dot-dot-dotted line corresponds to the power-law distribution. One can see that only the kappa distribution provides a reasonable fit of the observed curve.

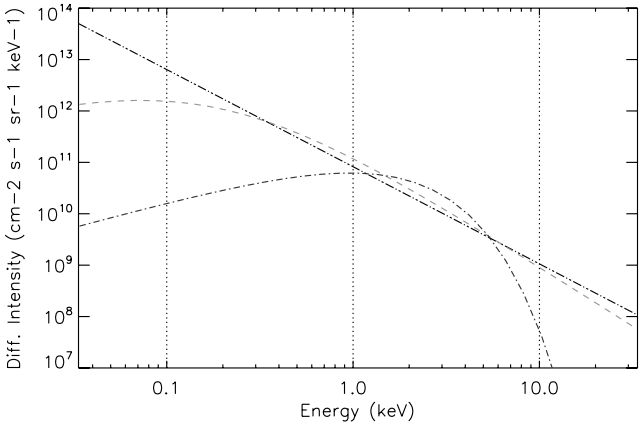

Figure 8. Energy spectra computed with the best fit parameters shown in Table 3. The dashed line represents the kappa distribution, the dash-dotted line represents the Maxwellian distribution and the dash-dot-dot-dotted line represents the power-law distribution. In order to compute the differential intensities, the curtain width is assumed to be 200 km wide.

them with the observations. Figure 8 presents the best fit energy spectra used to compute the corresponding emission profiles. One can note that only the kappa distribution generates a vertical profile compatible with the observations. The profiles that we used for the best fit lie approximately 20° away from the main spot. We also perform the same analysis with profiles taken approximately 40° away from the main spot (not shown here). Since the brightness is lower and only 19 images are used, the signal to noise ratio is lower but the results are very similar and are presented between brackets in Table 3.

4.3. Tail Brightness

[24] The extracted vertical profiles also make it possible to measure the tail brightness as a function of the longitude angle between the profile and the main spot. Figure 9 shows the evolution of the maximum tail brightness with the distance from the spot. To compare these brightnesses, the tail is considered to be perpendicular to the line of sight. Consequently, the image brightness is corrected for the sine of the angle between the curtain direction and the line of sight. The least squares fit of the brightness variation with an exponential law has an e-folding length of 21,000 km and is shown on the same figure. This value is ~4 times bigger than the distance derived by *Hill and Vasyliūnas* [2002]. However, their estimate is based on the first 15,000 kilometers of the tail while our measurement includes points located twice further. Considering that the latitudinal width of the tail is equal to Io's diameter as mapped along the field lines, we estimate the energy flux injected into the tail to be between 2 and 20 mW/m^2.

5. Discussion

[25] We developed a new method to automatically identify the planetary limb on the images. Since the technique has been validated on Saturn with an independent method, we applied our method to the entire dataset to compute the planetary center on each image. The large amount of data

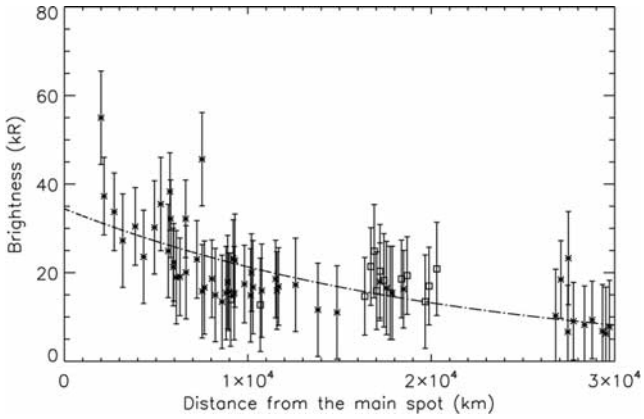

Figure 9. Maximum brightness as a function of the distance from the considered cuts to the IFP main spot location as described by our new reference contours. Note that this brightness is measured as seen from HST and does not correspond to the brightness an observer would see, when looking down vertically on the emission point. Northern hemisphere observations are represented by stars while southern hemisphere ones are represented by squares. The dash-dotted line is the least squares best fit with an exponential law.

collected during the HST/New Horizons campaign provided images of the Io footprint over a wide range of System III longitudes. *Grodent et al.* [2008] carefully measured these footprint locations in order to build reference contours for the different satellite footprints in the northern hemisphere. However, the poor accuracy of the IFP locations around 0° S3 made the contour difficult to close in a reasonable way in the $0-60°$ range. We took advantage of IFP images with identical Io S3 latitudes but with different local time configurations to precisely locate the IFP for these critical longitudes. Finally, we constructed IFP reference contours for both hemispheres based on these IFP locations.

[26] The new reference contours describing the IFP path were then used to compute the angle between the S3 location of Io and the projection of the IFP along the unperturbed magnetic field lines. Figure 3 shows that the lead angles vary with the S3 position of Io but are very model dependent. Additionally, in the northern hemisphere, the lead angles do not organize in a smooth trend, whatever the model. Even though the southern hemisphere curve shows some regularity, it implies that the lead angle when Io is in the dense torus center can vary from $\sim$0° to $\sim$9°. We note that the lead angles vary with Io's longitude but do not follow the ideal Alfvén wing model expectations. In this interpretation framework, the maximum lead angle is supposed to occur when the Alfvén waves have to cross the entire torus, while the minimum value is expected when the Alfvén waves propagate through a relatively short path in the torus. It is thus surprising to find that the lead angle could reach both its minimum and maximum values when Io is exactly in the same position relative to the torus.

[27] These results and the strong model dependence suggest that the current magnetic field models may not be accurate enough to provide trustworthy lead angle estimates. Possibly, future JUNO probe magnetic field observations will have the required precision for such measurements. Furthermore, the fact that inter-spot distances follow symmetric and regular curves when measured directly on the planet strengthens this conclusion. If the Alfvénic disturbance can be assumed to be linear, the inter-spot distances are related to the bending of the Alfvén wing. Then the secondary spot cannot be attributed to Alfvén wing reflections at the plasma torus boundaries because the distance would not be a minimum when Io is in the torus center. Only the trans-hemispheric electron beam scenario could explain the secondary spot behavior. In this case, the lead angle varies with Io's centrifugal latitude, and its maximum value corresponds to the maximum inter-spot distance and lies around 4°. However, Alfvén wing reflections could still account for the third spot as suggested by *Bonfond et al.* [2008]. If non-linear wave interactions are significant, then the link between the lead angle and the inter-spot distance is less direct. Further simulations are required to test whether such models can better match the inter-spot distances reported here.

[28] The average altitude at the emission peak derived from vertical profiles is 900 km ± 125 km. This peak altitude is fairly constant with the distance from the main spot, which indicates that the precipitating electron energy is relatively stable all along the tail. The decrease of the tail brightness shown in Figure 9 is most likely attributable to a drop in the particle flux, as suggested by color ratio measurements [*Gérard et al.*, 2002]. However, the color ratio measurements only extend down to 20° downstream of the main spot while our data span the range from 4° to 60°. Figure 9 shows that the tail brightness appears to decrease faster close to Io than further downstream. This difference may be partly attributed to a contamination from emissions coming from secondary spots in the first few thousand kilometers. Nevertheless, it could also be consistent with models expecting the wake plasma velocity lag to decrease quickly before reaching an exponential regime. The injected energy fluxes inferred from the tail brightness lie between 2 and 20 mW/m^2 and are slightly higher than those predicted by *Ergun et al.* [2009]. Assuming that the precipitating electron population is mono-energetic, the energy corresponding to 900 km is 2 keV if we consider the heated atmosphere from *Grodent et al.* [2001]. On the other hand, *Gérard et al.* [2002] concluded that IFP electrons would have a typical energy of $\sim$55 keV under the assumption that the methane vertical profile and the pressure-altitude relationship at the North Equatorial Band (NEB) [*Gladstone et al.*, 1996] also applies to the polar regions. However, *Grodent et al.* [2001] showed that the thermal structure of the atmosphere is significantly modified by the auroral energy input. We note that our mean value is much lower than estimates inferred from color ratio measurements, but is closer to the energy that electrons would acquire in the 1 kV potential drop computed by *Ergun et al.* [2009].

[29] Nevertheless, the constant 430 km scale height of the vertical emission profiles indicates that the precipitating electron distributions can be neither mono-energetic nor Maxwellian. In the Earth's aurora, mono-energetic distributions are usually linked to inverted-V structures, where the electrons are accelerated by quasi-static potential drops. Maxwellian distributions are most often associated with isotropically heated populations. As expected, a power-law overestimates either the low energy part of the spec-

trum, if the spectral index is too high, or the high energy part in the opposite case, and it never produces a peaked curve resembling the observations. In the IFP tail case, the only distribution that reasonably reproduces the observations is a kappa distribution with a relatively low characteristic energy. Such broad energy distribution could be related to electron acceleration by inertial Alfvén waves [*Ergun et al.*, 2006; *Swift*, 2007]. The inertial Alfvén modes arise when one takes finite electron inertia into account in obtaining the dispersion relation and when the perpendicular wavelength of the Alfvén wave is on the order of the local electron skin depth [*Jones and Su*, 2008]. Sensitivity tests performed either for the NEB atmosphere or for an empirical very hot atmosphere showed that the characteristic energies could change by a factor of four at most. However, vertical profiles produced by mono-energetic or Maxwellian distributions would never be as extended as observed, whatever the atmospheric model we use. Similarly, shifting the profile by 120 km up or down could change the mean energies by a factor of two at most, but the conclusions on the best energy distribution would remain unchanged as well. Consequently, even if the predicted energy flux and the particle mean energy are reasonable, the assumption that electrons are accelerated by a localized static electric field as proposed by *Ergun et al.* [2009] does not seem to be in agreement with the vertical extent of the emission profile. Incidentally, we note that the κ spectral index we infer from our calculations is very similar to the $\kappa = 2.4$ value measured in the plasma torus by Ulysses [*Meyer-Vernet et al.*, 1995]. However, an initial kappa population further accelerated through a static electric potential would lack low energy electrons, contradicting our observations.

[30] Even if the definitive explanation is out of the scope of this paper, two possible reasons could be invoked to reconcile the high emission peak altitude and the weak but undeniable methane absorption in FUV spectra. First of all, energies derived from color ratio measurements assume a Maxwellian distribution of the precipitating electrons. We show here that a broader energy spectrum is needed to fit the observations. This implies that part of the impinging electrons can penetrate deep into the atmosphere, while another part will lose most of its energy in the upper atmosphere. Thus the observed absorption could result from the combination of strong absorption of the emissions caused by the more energetic particles and weak or no absorption of the high altitude emissions. The use of an auroral heated atmosphere as proposed by *Grodent et al.* [2001] could also help raise the methane homopause. Moreover, their 1D model only takes the diffusion of atmospheric particles into account, and does not consider 3D convective phenomena. Thus, the second possibility is that vertical winds triggered by auroral precipitation could also transport hydrocarbon molecules from the near homopause region to higher altitudes. The energy input should be on the order of the total thermal energy in the atmospheric column to generate convection [*Smith*, 1998]. At an altitude of 900 km, this thermal energy is equal to $\sim$125 J for a 1 m^2 cross section column. Consequently, assuming that tail precipitating energy flux is on the order of 10 mW/m^2, approximately 3.5 hours are required to provide this amount of energy. In a reference frame fixed to Jupiter, Io moves by $\sim 100^\circ$ during this time interval. Strictly speaking, this would mean that convection is likely to take place above 900 km, but would be established in the downstream part of the tail only. However several points need to be taken into account that could mitigate this statement and lead to faster and deeper convection. First, we neglected the impact of the spots which are at least 10 times brighter than the tail. Secondly, we did not consider the fact that a point on the reference contour is heated repeatedly for 3.5 hours every Io rotation, i.e. approximately every 13h. Thirdly, we neglected Joule heating associated with Pedersen currents. And finally, it must be noted that the estimator provides the order of magnitude required to establish some convection, but does not replace a dynamic and self consistent 3D analysis of the impact of the IFP on Jupiter's upper atmosphere. Furthermore, a full 3D analysis would also take into account additional energy transport mechanisms like conduction, horizontal advection and radiation, which may possibly mitigate or suppress the onset of convection. Further studies are needed to determine if and how convection takes place and whether it would originate deep enough to raise the hydrocarbon molecules.

6. Conclusions

[31] The main results of the present study can be summarized as follows:

[32] 1. Comparison between the erratic and unexpected behavior of the equatorial lead angle and the regular and smooth evolution of the inter-spots distances suggests that the current magnetic field models are not sufficiently accurate to provide information on the Alfvén wing's bending.

[33] 2. The correlation between the inter-spot distances and the centrifugal latitude of Io, together with the symmetric behavior of the curves in the northern and southern hemispheres, suggests that the secondary spot is not attributable to Alfvén wing reflections at the torus boundaries. However, our measurements are compatible with the trans-hemispheric electron beams model.

[34] 3. The IFP tail lies $\sim$900 km above the limb, which suggests that the involved electrons have a mean energy around 1–2 keV.

[35] 4. The shape of the observed vertical emission profiles is too wide to be explained by a mono-energetic distribution of the precipitating electrons. Using the auroral heated atmosphere from *Grodent et al.* [2001], the best fit is obtained for a kappa distribution with a characteristic energy of $\sim$70 eV, a spectral index of 2.3 and a mean energy $\simeq$1 keV. Additionally, the peak altitude and the profile vertical width are not evolving significantly along the tail, while the brightness is decreasing.

[36] **Acknowledgments.** The authors thank D. Bisikalo and V. Shematovich for their help concerning the Monte Carlo model and B. Hubert for helpful discussions. B.B. was supported by the PRODEX program managed by ESA in collaboration with the Belgian Federal Science Policy Office. J.C.G., D.G. and A.R. are funded by the Belgian Fund for Scientific Research (FNRS). Work in Boston was supported by grants HST-GO-10862.01-A and HST-GO-10507.01-A from the Space Telescope Science Institute to Boston University. This research is based on observations made with the Hubble Space Telescope obtained at the Space Telescope Science Institute, which is operated by AURA Inc.

[37] Wolfgang Baumjohann thanks Nicholas Achilleos and Ashwin Vasavada for their assistance in evaluating this paper.

References

Boffi, F. R., M. Sirianni, R. A. Lucas, N. R. Walborn, and C. R. Proffitt (2008), Delivery of a new ACS SBC throughput curve for Synphot, *Tech. Rep. ACS 2008-002*, 9 pp., Space Telesc. Sci. Inst., Baltimore, Md.

Bonfond, B., J.-C. Gérard, D. Grodent, and J. Saur (2007), Ultraviolet Io footprint short timescale dynamics, *Geophys. Res. Lett.*, *34*, L06201, doi:10.1029/2006GL028765.

Bonfond, B., D. Grodent, J.-C. Gérard, A. Radioti, J. Saur, and S. Jacobsen (2008), UV Io footprint leading spot: A key feature for understanding the UV Io footprint multiplicity?, *Geophys. Res. Lett.*, *35*, L05107, doi:10.1029/2007GL032418.

Clarke, J. T., D. Grodent, S. W. H. Cowley, E. J. Bunce, P. Zarka, J. E. P. Connerney, and T. Satoh (2004), Jupiter's aurora, in *Jupiter. The Planet, Satellites and Magnetosphere*, *Cambridge Planet. Sci.*, vol. 1, edited by F. Bagenal, T. E. Dowling, and W. B. McKinnon, pp. 639–670, Cambridge Univ. Press, Cambridge, U. K.

Clarke, J. T., et al. (1996), Far-ultraviolet imaging of Jupiter's aurora and the Io footprint, *Science*, *274*, 404–409, doi:10.1126/science.274.5286.404.

Clarke, J. T., et al. (1998), Hubble Space Telescope imaging of Jupiter's UV aurora during the Galileo orbiter mission, *J. Geophys. Res.*, *103*(E9), 20,217–20,236.

Clarke, J. T., et al. (2002), Ultraviolet emissions from the magnetic footprints of Io, Ganymede and Europa on Jupiter, *Nature*, *415*, 997–1000.

Connerney, J. E. P., R. Baron, T. Satoh, and T. Owen (1993), Images of Excited H_3^+ at the Foot of the Io Flux Tube in Jupiter's Atmosphere, *Science*, *262*, 1035–1038, doi:10.1126/science.262.5136.1035.

Connerney, J. E. P., M. H. Acuña, N. F. Ness, and T. Satoh (1998), New models of Jupiter's magnetic field constrained by the Io flux tube footprint, *J. Geophys. Res.*, *103*(A6), 11,929–11,940.

Crary, F. J., and F. Bagenal (1997), Coupling the plasma interaction at Io to Jupiter, *Geophys. Res. Lett.*, *24*(17), 2135–2138.

Dalgarno, A., M. Yan, and W. Liu (1999), Electron energy deposition in a gas mixture of atomic and molecular hydrogen and helium, *Astrophys. J. Supp.*, *125*, 237–256, doi:10.1086/313267.

Delamere, P. A., F. Bagenal, R. Ergun, and Y.-J. Su (2003), Momentum transfer between the Io plasma wake and Jupiter's ionosphere, *J. Geophys. Res.*, *108*(A6), 1241, doi:10.1029/2002JA009530.

Ergun, R. E., Y.-J, Su, L. Andersson, F. Bagenal, P. A. Delemere, R. L. Lysak, and R. J. Strangeway (2006), *S* bursts and the Jupiter ionospheric Alfvén resonator, *J. Geophys. Res.*, *111*, A06212, doi:10.1029/2005JA011253.

Ergun, R. E., L. Ray, P. A. Delamere, F. Bagenal, V. Dols, and Y.-J. Su (2009), Generation of parallel electric fields in the Jupiter-Io torus wake region, *J. Geophys. Res.*, *114*, A05201, doi:10.1029/2008JA013968.

Frank, L. A., W. R. Paterson, K. L. Ackerson, V. M. Vasyliunas, F. V. Coroniti, and S. J. Bolton (1996), Plasma observations at Io with the Galileo spacecraft, *Science*, *274*, 394–395, doi:10.1126/science.274.5286.394.

Garvey, R. H., and A. E. S. Green (1976), Energy-apportionment techniques based upon detailed atomic cross sections, *Phys. Rev. A*, *14*, 946–953, doi:10.1103/PhysRevA.14.946.

Garvey, R. H., H. S. Porter, and A. E. S. Green (1977), An analytic degradation spectrum for H_2, *J. Appl. Phys.*, *48*, 190–193, doi:10.1063/1.323308.

Gérard, J.-C., J. Gustin, D. Grodent, P. Delamere, and J. T. Clarke (2002), Excitation of the FUV Io tail on Jupiter: Characterization of the electron precipitation, *J. Geophys. Res.*, *107*(A11), 1394, doi:10.1029/2002JA009410.

Gérard, J.-C., A. Saglam, D. Grodent, and J. T. Clarke (2006), Morphology of the ultraviolet Io footprint emission and its control by Io's location, *J. Geophys. Res.*, *111*, A04202, doi:10.1029/2005JA011327.

Gérard, J.-C., B. Bonfond, J. Gustin, D. Grodent, J. T. Clarke, D. Bisikalo, and V. Shematovich (2009), Altitude of Saturn's aurora and its implications for the characteristic energy of precipitated electrons, *Geophys. Res. Lett.*, *36*, L02202, doi:10.1029/2008GL036554.

Gladstone, G. R., M. Allen, and Y. L. Yung (1996), Hydrocarbon photochemistry in the upper atmosphere of Jupiter, *Icarus*, *119*, 1–52, doi:10.1006/icar.1996.0001.

Goldreich, P., and D. Lynden-Bell (1969), Io, a Jovian unipolar inductor, *Astrophys. J.*, *156*, 59–78, doi:10.1086/149947.

Grodent, D., J. H. Waite, Jr., and J.-C. Gérard (2001), A self-consistent model of the Jovian auroral thermal structure, *J. Geophys. Res.*, *106*(A7), 12,933–12,952.

Grodent, D., B. Bonfond, J.-C. Gérard, A. Radioti, J. Gustin, J. T. Clarke, J. Nichols, and J. E. P. Connerney (2008), Auroral evidence of a localized magnetic anomaly in Jupiter's northern hemisphere, *J. Geophys. Res.*, *113*, A09201, doi:10.1029/2008JA013185.

Hill, T. W., and V. M. Vasyliūnas (2002), Jovian auroral signature of Io's corotational wake, *J. Geophys. Res.*, *107*(A12), 1464, doi:10.1029/2002JA009514.

Jackman, C. H., R. H. Garvey, and A. E. S. Green (1977), Electron impact on atmospheric gases: I. Updated cross sections, *J. Geophys. Res.*, *82*(32), 5081–5090.

Jacobsen, S., J. Saur, F. M. Neubauer, and N. Schilling (2007), Effects of a nonlinear treatment of Io's interaction with the Jovian magnetosphere, *Eos Trans. AGU*, *88*(52), Fall Meet. Suppl. Abstract P51A-0207.

Jones, S. T., and Y.-J. Su (2008), Role of dispersive Alfvén waves in generating parallel electric fields along the Io-Jupiter fluxtube, *J. Geophys. Res.*, *113*, A12205, doi:10.1029/2008JA013512.

Knight, S. (1973), Parallel electric fields, *Planet. Space Sci.*, *21*, 741–750, doi:10.1016/0032-0633(73)90093-7.

Meyer-Vernet, N., M. Moncuquet, and S. Hoang (1995), Temperature inversion in the Io plasma torus, *Icarus*, *116*, 202–213, doi:10.1006/icar.1995.1121.

Neubauer, F. M. (1980), Nonlinear standing Alfvén wave current system at Io: Theory, *J. Geophys. Res.*, *85*(A3), 1171–1178.

Pontius, D. H. (2002), The Io current wing, *J. Geophys. Res.*, *107*(A8), 1165, doi:10.1029/2001JA000331.

Prangé, R., D. Rego, D. Southwood, P. Zarka, S. Miller, and W. Ip (1996), Rapid energy dissipation and variability of the Io-Jupiter electrodynamic circuit, *Nature*, *379*, 323–325, doi:10.1038/379323a0.

Prangé, R., D. Rego, L. Pallier, J. Connerney, P. Zarka, and J. Queinnec (1998), Detailed study of FUV Jovian auroral features with the post-COSTAR HST faint object camera, *J. Geophys. Res.*, *103*(E9), 20,195–20,216.

Saur, J. (2004), A model of Io's local electric field for a combined Alfvénic and unipolar inductor far-field coupling, *J. Geophys. Res.*, *109*, A01210, doi:10.1029/2002JA009354.

Saur, J., F. M. Neubauer, J. E. P. Connerney, P. Zarka, and M. G. Kivelson (2004), Plasma interaction of Io with its plasma torus, in *Jupiter. The Planet, Satellites and Magnetosphere*, *Cambridge Planet. Sci.*, vol. 1, edited by F. Bagenal, T. E. Dowling, and W. B. McKinnon, pp. 537–560, Cambridge Univ. Press, Cambridge, U. K.

Shematovich, V. I., D. V. Bisikalo, J.-C. Gérard, C. Cox, S. W. Bougher, and F. Leblanc (2008), Monte Carlo model of electron transport for the calculation of Mars dayglow emissions, *J. Geophys. Res.*, *113*, E02011, doi:10.1029/2007JE002938.

Shyn, T. W., and W. E. Sharp (1981), Angular distributions of electrons elastically scattered from H_2, *Phys. Rev. A*, *24*, 1734–1740, doi:10.1103/PhysRevA.24.1734.

Smith, R. W. (1998), Vertical winds: A tutorial, *J. Atmos. Sol. Terr. Phys.*, *60*, 1425–1434, doi:10.1016/S1364-6826(98)00058-3.

Swift, D. W. (2007), Simulation of auroral electron acceleration by inertial Alfvén waves, *J. Geophys. Res.*, *112*, A12207, doi:10.1029/2007JA012423.

Vasavada, A. R., A. H. Bouchez, A. P. Ingersoll, B. Little, C. D. Anger, and The Galileo SSI Team (1999), Jupiter's visible aurora and Io footprint, *J. Geophys. Res.*, *104*(E11), 27,133–27,142.

B. Bonfond, J.-C. Gérard, D. Grodent, and A. Radioti, Laboratoire de Physique Atmosphérique et Planétaire, Université de Liège, Allée du 6 Août 17, B-4000 Liège, Belgium. (b.bonfond@ulg.ac.be)

J. T. Clarke, Department of Astronomy and Center for Space Physics, Boston University, 725 Commonwealth Avenue, Boston, MA 02215, USA.

P. A. Delamere and V. Dols, Laboratory for Atmospheric and Space Physics, University of Colorado, Boulder, CO 80303, USA.